Precise simulation of single-hole spin control in quantum dots

YuanDong Wang, JingHan Ni, and JianHua Wei*
Department of Physics, Renmin University of China, Beijing 100872, China
(Received 12 May 2017; revised manuscript received 14 December 2017; published 28 December 2017)

The initialization, control, and readout of a single-hole spin qubit is precisely simulated by accurately solving the extended Anderson impurity model in the real-time domain with the hierarchical equations of motion approach. The initialization is realized by ionization of an exciton with high fidelity. Then, a SU(2) control is achieved via the combination of Larmor precession of the hole spin in Voigt geometry magnetic field and rotation about the optical axis with a geometric phase. Finally, the readout of the qubit is implemented through photocurrent recording. Our theory not only reproduces the recent experimental results with one set of internal parameters but also predicts a maximal fidelity by adjusting the dot-electrode coupling strength.

DOI: 10.1103/PhysRevB.96.245426

I. INTRODUCTION

A trapped single spin in quantum dots (QDs) is a promising qubit that can be optically controlled within a picosecond [1–3]. It is also compatible with the present large-scale integrated circuit in quantum information processing (QIP). In the literature, many achievements have been made in QD-based electron spin qubits [2,4,5]. However, the non-Markovian hyperfine interaction can induce decoherence and decrease the fidelity of electron spin control [6]. In order to overcome this shortcoming, much attention has been paid to the hole spin qubit since the valence-band holes possess a p-type wave function that leaves a small residual dipolar interaction [7], which may highly suppress contact hyperfine interaction and produce much longer lifetimes [8,9]. In addition, the large spin-orbit coupling from the p-type valence state makes decoherence sensitive to electric fields [3], which provides a more convenient way to control hole spin. Recently, many experiments on single-hole spin qubits have been performed, including initialization, coherent control, and readout [3,10–13].

For realistic application of hole spin qubits, a high fidelity during the initializing process is a key requirement. Among the proposed schemes at present, ionization of an exciton has distinct advantages, which can achieve a fidelity of 98.5% [10]. By reducing fine-structure splitting or applying a magnetic field parallel to the growth direction, fidelity as high as 99% is possible [14,15]. Moreover, it is fast (in picseceonds) enough to meet another requirement that the initialization time should be an order of 10^{-4} smaller than the decoherence time. As a comparison, optical pumping [2], one of the other schemes, reaches a fidelity of only 95% on the time scale of nanoseconds [16].

Whereas experimental investigations have been actively performed, theoretical works on the hole spin qubit are not sufficient so far. The rate equation is a commonly used method to simulate the hole spin manipulation in the literature [17]. We comment that it is not accurate enough due to the following two defects. First, in the QD-based hole spin qubit, the QD directly couples to electrodes (metal leads), which makes the qubit a typical quantum open system with infinite degrees of freedom, while the rate equation concerns only the diagonal terms of the reduced density matrix and treats the dot-electrode couplings with low-order perturbation schemes. Second, the QD-based hole spin qubit is also a typical strongly correlated system with electron-electron (e-e), hole-hole (h-h), and electron-hole (e-h) interactions, while the rate equation either neglects those important interactions or treats them on the mean-field level.

Obviously, for a theoretical study on hole spin qubits, a nonperturbative approach beyond the rate equation is highly required. In the present work, we adopt the hierarchical equations of motion (HEOM) approach, which nonperturbatively resolves the combined effects of dot-electrode dissipation, Coulomb interactions, and non-Markovian memory [18–21]. As an accurate impurity solver, the HEOM approach has been used to deal with various impurity problems, such as Kondo problems [19,22,23], and nonequilibrium transport with many-body effects [24,25]. The extended Anderson impurity model will be used to describe the hole spin qubit, with the Coulomb interactions and dot-electrode couplings being fully considered. Then, this quantum model will be treated by the HEOM approach nonperturbatively in the real-time domain to precisely simulate the single-hole spin manipulation.

In what follows, the whole process of QIP, including initialization, coherent control, and readout, will be precisely simulated. As will be demonstrated, our theory not only reproduces the recent experimental results in Ref. [13] with one set of internal parameters but also predicts a maximal fidelity by adjusting the dot-electrode coupling strength.

The complete process of qubit initialization, coherent control, and readout is sketched in Figs. 1(a) and 1(b). In order to initialize the single-hole spin, a σ_+ resonant circularly polarized pulse with a pulse area of π is applied to create an e-h pair and drive the ground state $|cgs\rangle$ (crystal ground state) into a neutral exciton state $|X^0_{\uparrow\Downarrow}\rangle$. The much larger effective mass of holes results in a much smaller hybridization strength than that of electrons, i.e., $\Delta_H \ll \Delta_E$. As a consequence, electrons in the conduction level tunnel into an electrode 2–3 orders of time magnitude faster than holes, which turns $|X^0_{\uparrow\Downarrow}\rangle$ into a single-hole spin state $|\Downarrow\rangle$ quickly. Then, an in-plane magnetic field B_x drives the single-hole spin to precess along the x axis to perform a U(1) operation. In order to realize a SU(2) operation in the Bloch sphere, the geometric-phase approach is adopted, as proposed in Ref. [26]. After a geometric pulse with a hyperbolic secant envelope, the hole spin undergoes a cycle from a single-hole to positive trion state and then back

*wjh@ruc.edu.cn

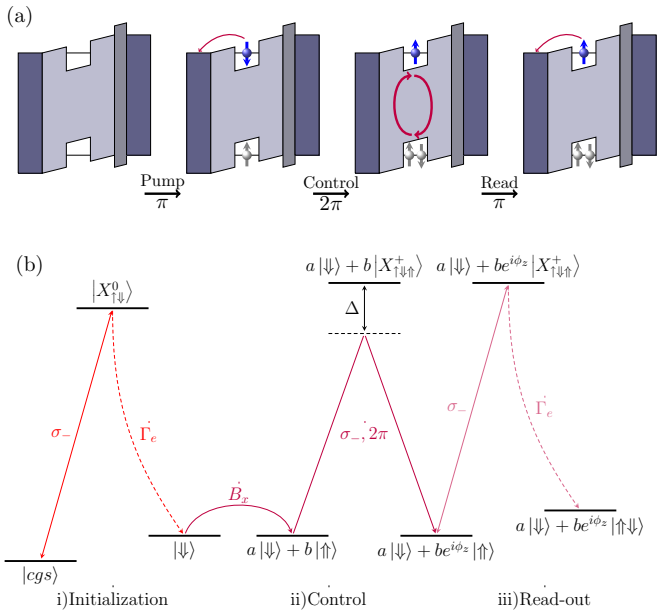

FIG. 1. (a) Schematic illustration of the single-hole spin control process. (b) Initialization, coherent control, and readout of a single-hole spin, where the solid arrows represent the optical excitation processes and the dashed ones indicate the transitions due to tunneling.

to a single-hole state, with a rotation angle ϕ_z acquired. After the control sequence, a detection circularly polarized pulse σ_+ is applied, which partially excites the single-hole state to a positive trion state. That process produces a photocurrent proportional to the spin-down component of the hole spin state, which can be used as qubit readout, called the photocurrent detection technique [27].

II. METHODOLOGY AND MODEL

With reference to experimental setups, our single-hole spin qubit consists of a QD connected to two electrodes (reservoirs), which can be described by the extended Anderson impurity Hamiltonian with e-e, h-h, and e-h interactions. The total Hamiltonian is written as

$$H = H_c + H_v + H_{c-v} + H_{\rm opt} + H_{\rm res} + H_{\rm dot-res}, \quad (1)$$

where H_c and H_v describe the conduction and valence levels with e-e and h-h interactions, respectively,

$$H_c = \sum_\mu \epsilon_c \hat{n}_{c\mu} + U_c \hat{n}_{c\uparrow}\hat{n}_{c\downarrow}, \quad (2)$$

$$H_v = \sum_\mu \epsilon_v \hat{n}_{v\mu} + U_v(1-\hat{n}_{v\uparrow})(1-\hat{n}_{v\downarrow}). \quad (3)$$

In the above equations, $\hat{n}_{c\mu} = \hat{a}^\dagger_{c\mu}\hat{a}_{c\mu}$ and $\hat{n}_{c\mu} = \hat{a}^\dagger_{c\mu}\hat{a}_{c\mu}$, where $\hat{a}_{c\mu}$ ($\hat{a}^\dagger_{c\mu}$) annihilates (creates) a conduction-level state with μ being spin ($\mu = \uparrow, \downarrow$).

As shown in the above equations, the Hamiltonian of the valence level is similar to that of the conduction one. That point needs to be clarified since different types of holes, heavy and light holes, may play different roles in experiments. As a reasonable approximation, we account for only one kind in our theory. Let us explain the reason as follows. First, the heavy holes ($m^{hh}_z = \pm 3/2$) and light holes ($m^{lh}_z = \pm 1/2$) in the valence band are degenerate in bulk semiconductors but are split in QDs because of their different confinement energy. This splitting makes it possible to consider only the heavy-hole manifolds. Then the heavy hole can be treated as a pseudo-spin-1/2, with a perturbative treatment of the heavy-light-hole mixing. The heavy hole is the one used in most hole spin qubit experiments. Second, an electron-hole pair forming an exciton has four possible spin values: $S_z = m^h_z + m^e_z = -2, -1, +1, +2$. Since the absorption of a single photon makes a change in angular momentum of ± 1, only the excitons with $S_z = \pm 1/2$ are optically allowed, while those with $S_z = \pm 2$ are forbidden due to the angular momentum conservation. From this point of view, it is reasonable to treat heavy and light holes as a 1/2 spin uniformly. As is well known, the heavy and light holes have much different effective masses at the Γ point, which will lead to different coupling strengths to electrodes. The splitting as well as the heavy-light-hole mixing will be further investigated in future research.

In our Hamiltonians, U_c (U_v) is the Coulomb repulsion energy if the c level (v level) is double (zero) occupied. The term

$$H_{c-v} = -\sum_{\mu,\mu'} U_{\rm exc}\hat{n}_{c\mu}(1-\hat{n}_{v\mu'}) \quad (4)$$

accounts for the Coulomb attraction in the e-h pair. $H_{\rm opt}$ denotes the interaction between the control field and QD, whose explicit expression will be specified later. The electrodes are modeled by noninteraction electrons

$$H_{\rm res} = \sum_{\alpha k\mu}(\epsilon_{\alpha k} + \mu_\alpha)\hat{d}^\dagger_{\alpha k\mu}\hat{d}_{\alpha k\mu}, \quad (5)$$

where $\hat{d}_{\alpha k\mu}$ ($\hat{d}^\dagger_{\alpha k\mu}$) denotes the creation (annihilation) operator of an electron in the specified α-electrode spin-orbital state $|k\mu\rangle$ of energy $\epsilon_{\alpha k}$. The nonequilibrium chemical potential μ_α, with $\alpha = L, R$, will arise in the presence of bias of voltage. The zero-energy point is set at the equilibrium chemical potential $\mu^{eq}_\alpha = 0$. The dot-electrode coupling is described by

$$H_{\rm dot-res} = \sum_{\alpha k\mu}(t_{c\alpha k}\hat{a}^\dagger_{c\mu}\hat{d}_{\alpha k\mu} + t_{v\alpha k}\hat{a}^\dagger_{v\mu}\hat{d}_{\alpha k\mu} + {\rm H.c.}). \quad (6)$$

It should be noted that due to the large effective mass of holes, the transfer-matrix element for the conduction level $t_{v\alpha k}$ is much smaller than that of the valence level $t_{c\alpha k}$. In the HEOM approach, the influence of electrodes on the QD acts through the hybridization functions with the Lorentzian form $\Delta_{\beta\gamma}(\omega) \equiv \sum_\alpha \Delta_{\alpha\beta\gamma}(\omega) = \pi \sum_{\alpha k} t_{\alpha\beta k}t^*_{\alpha\gamma k}\delta(\omega - \epsilon_{\alpha k}) = \Delta W^2/[(\omega-\mu_\alpha)^2 + W^2]$, where W is the bandwidth and μ_α is the chemical potential of lead α. The details of the HEOM formalism were developed in Refs. [18,19], and the final HEOM can be cast into the compact form

$$\dot{\rho}^{(n)}_{j_1\cdots j_n} = -\left(i\mathcal{L} + \sum_{r=1}^n \gamma_{j_r}\right)\rho^{(n)}_{j_1\cdots j_n} - i\sum_j \mathcal{A}_{\bar{j}}\,\rho^{(n+1)}_{j_1\cdots j_n j}$$
$$- i\sum_{r=1}^n (-)^{n-r}\,\mathcal{C}_{j_r}\,\rho^{(n-1)}_{j_1\cdots j_{r-1}j_{r+1}\cdots j_n}, \quad (7)$$

where the index $j \equiv (\sigma\mu n)$ corresponds to the transfer of an electron to or from ($\sigma = +$ or $-$) the impurity state and the Grassmannian superoperators $\mathcal{A}_{\bar{j}} \equiv \mathcal{A}^{\bar{\sigma}}_{\bar{\mu}}$ and $\mathcal{C}_{j_r} \equiv \mathcal{C}^{\sigma}_{\mu\nu m}$ are defined via their fermionic actions on an operator $\hat{O}$ as $\mathcal{A}^{\bar{\sigma}}_{\bar{\mu}}\hat{O} \equiv [\hat{a}^{\bar{\sigma}}_{\mu}, \hat{O}]$ and $\mathcal{C}^{\sigma}_{\mu\nu m}\hat{O} \equiv \eta^{\sigma}_{\mu\nu m}\hat{a}^{\sigma}_{\nu}\hat{O} + (\eta^{\bar{\sigma}}_{\mu\nu m})^{*}\hat{O}\hat{a}^{\sigma}_{\nu}$, respectively, with $\bar{\sigma}$ being the opposite sign of σ. The on-dot electron interactions are incorporated in the Liouvillian of impurities: $\mathcal{L}\cdot \equiv [H_{\rm dot}, \cdot]$. Here, $\rho_0(t) = \rho(t) = {\rm tr}_{\rm res}\rho_{\rm total}(t)$ is the reduced density matrix, and $\{\rho_{j_1\cdots j_n}(t)^n; n = 1, \ldots, L\}$ are auxiliary density matrices, with L denoting the truncation level. Usually, a relatively low L (say, $L = 4$ or 5) is sufficient to yield quantitatively converged results. Any observable $\hat{O}$ of the dot system can be calculated in the form of $\bar{O} = {\rm tr}(\rho_0\hat{O})$. The spectral functions of the impurity can be calculated based on a linear response theory established in the HEOM Liouville space [19]. For the ith impurity orbital, the spin-μ spectral function $A_{i\mu}(\omega)$ is evaluated via

$$A_{i\mu}(\omega) \equiv \frac{1}{2\pi}\int dt e^{i\omega t}\langle\{\hat{a}_{i\mu}(t), \hat{a}_{i\mu}(0)\}\rangle = \frac{1 + e^{-\omega/T}}{2\pi}\int dt e^{i\omega t}\langle\hat{a}_{i\mu}(t)\hat{a}_{i\mu}(0)\rangle \qquad (8)$$

and $A_i(\omega) = \sum_{\mu} A_{i\mu}(\omega)$. The transient current through the electrode α is determined by the first-tier auxiliary density operators as

$$I_{\alpha}(t) = e\frac{i}{\hbar^2}\sum_{i\mu}{\rm tr}_s\{\rho^{\dagger}_{\alpha\mu}(t)\hat{a}_{i\mu} - \hat{a}^{\dagger}_{i\mu}\rho^{-}_{\alpha\mu}(t)\}, \qquad (9)$$

where the index i sums from c to v to count the contributions of c and v levels. To simulate experiments, we choose parameters which can produce the same energy-level structure as those in experiments, i.e., $\epsilon_c = 2$ meV, $\epsilon_v = -2$ meV, $U_c = U_v = 2$ meV, $U_{\rm exc} = 1$ meV, and a reverse bias $V = \mu_L - \mu_R = 0.2$ meV.

The HEOM method is nonperturbative. It treats quantum impurity systems from the perspective of open dissipative dynamics. In principle, the HEOM formalism is formally exact for noninteracting electron reservoirs. It also resolves nonperturbatively the combined effects of e-e interactions; the HEOM theory is established based on the Feynman-Vernon path-integral formalism, in which all the system-bath correlations are taken into consideration. It is capable of characterizing both static and dynamical electronic properties under equilibrium and out-of-equilibrium conditions as well, and the HEOM is a high-accuracy numerical approach. It has the ability to achieve the same level of accuracy as the latest high-level numerical renormalization group (NRG) method. As for the disadvantages, the HEOM method works only at finite temperature and cannot deal with the zero-temperature case at present. In addition, the computational cost increases dramatically as the system temperature decreases. For a very low temperature, a higher truncation level is necessary to ensure numerical convergence, leading to rapid growth of the required computational resources.

III. RESULTS AND DISCUSSION

A. Initialization and maximum fidelity

In the initialization process, a resonant pulse with a π pulse area is applied continuously for 10 ps. Its Hamiltonian is $H_{\rm opt} = \Omega(e^{i\omega t}c^{\dagger}_{c\uparrow}c_{v\downarrow} + {\rm H.c.})$, where $\hbar\omega = 3$ meV, $\Omega = 0.1$ meV. The hybridization strengths are initially chosen to be $\Delta_E = 0.05$ meV and $\Delta_H = 0.0003$ meV. The time evolution of the occupation numbers of c and v levels is presented in Fig. 2(a). As shown, the maximum electron number in the c level is around 0.62 rather than unity, which is induced by the fast electron tunneling from the neutral exciton $|X_0\rangle$. At $t > 10$ ps, electron and hole occupation numbers will decay with different behaviors; that is, the former is exponential, but the latter is approximately linear, resulting from their different hybridization strengths to electrodes. The initialization will be accomplished in $t \sim 70$ ps, when the electron in the c level has almost totally escaped into the electrodes ($N_c \sim 0$) and the single-hole in the v level is almost fully occupied ($N_v \sim 1$). Figure 2(b) depicts this photocurrent during the initialization process. As shown, a peak of photocurrent forms at the end of the pulse ($t \sim 10$ ps), when the electron maximally accumulates in the c level. Since the charge-photocurrent in our theory is precisely conserved, the photocurrent shown in Fig. 2(b) is much larger than that in experiments.

Before discussing fidelity, let us clarify its different definitions. In experiments, the fidelity is convenient to determine via the measurable photocurrent, which is defined as $\tilde{F} = \frac{PC^{X^+}_{\rm cross}}{PC^{X^+}_{\rm cross} + PC^{X^+}_{co}}$ [14,15], where $PC^{X^+}_{\rm cross}$ and $PC^{X^+}_{co}$ are the amplitudes of the X^+ peaks in the cross- and copolarized pulse spectra. In the present work, we use a more theoretical definition, $\bar{F} = \langle\psi_{\rm in}|\hat{U}\hat{\rho_{\rm out}}\hat{U}|\psi_{\rm in}\rangle$ [28], which measures the distance between the real evolution U and the target evolution U_t to a given initial state $|\psi_{\rm in}\rangle$. $\tilde{F}$ and $\bar{F}$ may have different values, although they describe the same physical process. It should be noted that $\tilde{F}$ reflects the population difference between up and down hole spins. However, the single-hole spin space is only a subspace of the full Hilbert one during the initialization. The tunneling process for electrons and holes from conduction and valence bands to electrodes will dynamically destroy the integrity of the hole spin, which will decrease the fidelity in principle. That decoherence effect has been well reflected in $\bar{F}$ but not in $\tilde{F}$, which may be still high as long as the pulse is fast enough to avoid the up-down spin mixing induced by transverse magnetic field.

In experiments, in order to achieve a high fidelity, an AlGaAs barrier is applied to tailor the tunneling rate of electrons and holes, which effectively adjusts the conduction- and valence-level-electrode hybridization strengths Δ_E and Δ_H. To check this effect theoretically, we investigate the dynamics of fidelity $\bar{F}$ during the excitation-tunneling process at different Δ_E and Δ_H. The initial state is set at the ground state $|cgs\rangle$, and the target one is the single-hole state $|\Downarrow\rangle$, which can be reached by the two-step process shown in Fig. 1(b): (a) optically exciting $|cgs\rangle$ to a neutral exciton state $|X_0\rangle$ and (b) $|X_0\rangle$ decaying to the single-hole state $|\Downarrow\rangle$ through fast electron tunneling. For an ideal spin qubit with high fidelity, the ultrashort c-level electron lifetime and long v-level hole storage time (against electron refilling from electrodes) are

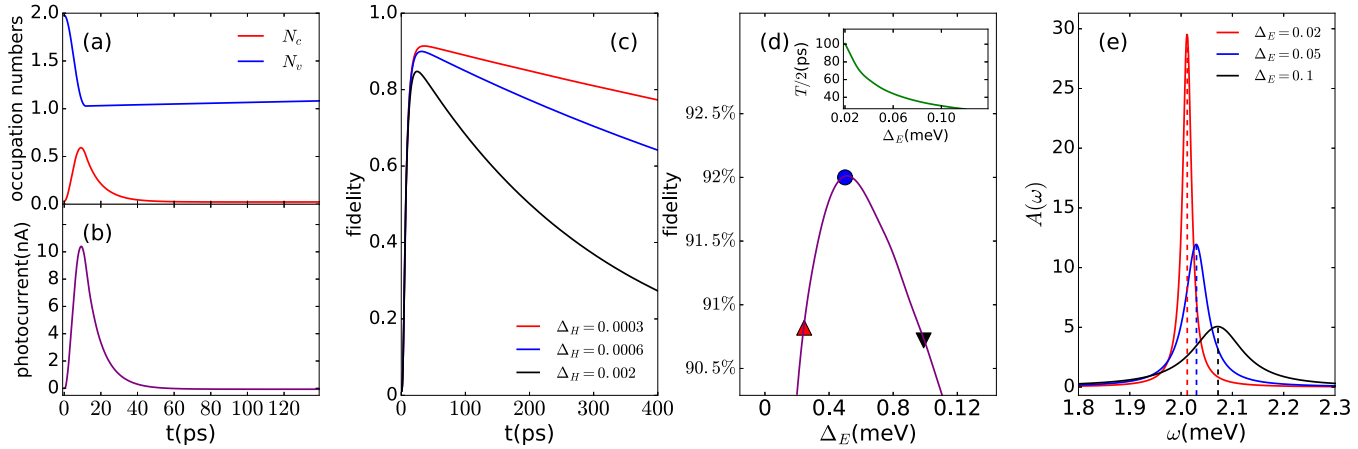

FIG. 2. Initialization process, with application of a σ_+ circularly polarized pulse tuned on resonance pulse. The pulse area is π, and the duration time $0 \leqslant t \leqslant 10$ ps. (a) The time evolution of occupation numbers of c level and v level. (b) The real-time photocurrent, with a maximum appearing at the end of the pulse ($t \sim 10$ ps). (c) Fidelity $\bar{F}$ as a function of time t at different hybridization strengths of the hole Δ_H with the excitation-tunneling process involved. (d) Fidelity $\bar{F}$ as a function of hybridization strength of Δ_E, with the maximum fidelity occurring at $\Delta_E \simeq 0.05$ meV. The inset shows the half Rabi cycle $T/2$ as a function of Δ_E. (e) The spectral functions of electrons at different Δ_E.

both required. Figure 2(c) shows the time evolution of fidelity with different Δ_H. Notice that electrons in electrodes tend to fill the hole through the whole process, even at the beginning of the optical excitation. With Δ_H decreasing, the hole storage time increases accordingly. At $\Delta_H = 0.0003$ meV, $\bar{F} \sim 93\%$ is obtained. If we calculate $\tilde{F}$ in this case, we can reproduce the high fidelity $\tilde{F} > 98\%$, in accordance with the observed values [10].

It seems that a very high initialization fidelity can be expected by simply increasing the electron hybridization strength Δ_E. However, when Δ_E is comparable to the frequency of the laser that has been tuned in resonance with the neutral exciton, it will inevitably bring damage to fidelity. One undesirable consequence is tunneling-induced dephasing, which was extracted in hole spin initialization at low temperature by Ardelt *et al.* [10]. We comment that the tunneling-induced dephasing has been intrinsically involved in HEOM calculations without additional parameter fitting. In Fig. 2(d), we depict the fidelity $\bar{F}$ as a function of Δ_E. As shown, with Δ_E increasing, the fidelity increases to a maximum of 92.1% at $\Delta_E = 0.052$ meV and then decreases. When $\Delta_E \simeq 173\Delta_H$, it begins to damage the fidelity and makes $\bar{F} < 90\%$ at $\Delta_E > 0.12$ meV. It should be noted that Δ_E can induce an energy-level shift [see Fig. 2(e)]; correspondingly, in order to maximize the fidelity, the frequency ω of the Rabi oscillation should be adjusted to satisfy the resonance condition. The half Rabi cycle as a function of Δ_E is shown in the inset of Fig. 2(d).

To further explain the peak structure of $\bar{F}$ shown in Fig. 2(d), we calculate the single-particle spectral function $A(\omega)$ of the c-level electron at $\Delta_E = 0.02$, 0.05, and 0.1 meV, and present the results in Fig. 2(e). Due to large Δ_E, $A(\omega)$ experiences a linewidth broadening, which may make the single-particle level invisible to optical excitation. The ground state $|cgs\rangle$ is only partly pumped to $|X_0\rangle$ within the adjacent area around zero detuning. The level broadening results in the broadening of photocurrent absorption spectra, which can be directly observed in experiments [10]. Another feature of $A(\omega)$ shown in Fig. 2(e) is the peak shift. At small Δ_E ($\Delta_E = 0.02$ meV), the peak is centered at $\omega \simeq 2.0$ meV, which is exactly the single-particle excitation energy in the c-level electron tunneling event. When Δ_E increases to 0.1 meV, the center of the peak shifts to 2.08 meV; meanwhile, the fidelity drops to 90.6%.

B. Coherent control and readout

A U(1) rotation for the initialized hole spin state can be achieved by applying a magnetic field B_x perpendicular to the growth direction (the Voigt geometry). The down-spin state $|\Downarrow\rangle$ is a superposition of the hole spin eigenstates in the x direction, which will perform Larmor precession about B_x at the frequency f_L determined by the hole Zeeman splitting. To detect the single-hole spin, a co- or cross-circularly polarized pulse with π pulse area is used to excite the single-hole to the positive trion state $|X^+\rangle$, which arrives following a time delay of τ_d after the preparation pulse. The resonance frequency of the detection pulse is positively detuned by comparison with that of the initialization one due to the additional e-h pair interaction U_{exc}. To demonstrate the photocurrent detection of a hole spin, we depict the time evolution of the photocurrent in Fig. 3(a), where σ_+ and σ_- denote the cocircular and cross-circular excitations, respectively. The detection pulse arrives following the time delay $\tau_d = \pi/f_L$, when the initialized down-spin hole state $|\Downarrow\rangle$ has precessed to the up-spin one $|\Uparrow\rangle$. At that time, the excitation of the cocircular detection pulse is completely suppressed; nevertheless, the cross-circular one is still optically active, as shown in Fig. 3(a).

In experiments, the polarization of a hole spin can be conveniently read out via observable photocurrent, $\tilde{S}_z = \frac{I_{\sigma-} - I_{\sigma+}}{I_{\sigma-} + I_{\sigma+}}$ [13], where $I_{\sigma\pm}$ is the value of the photocurrent peak for the detection pulse $\sigma_\pm$. In our theory, the exact z component of the hole spin can be obtained through $\bar{S}_z = \text{tr}(\rho \hat{S}_z)$, which can be used to examine the accuracy of the photocurrent readout technique. Figure 3(b) shows a comparison between

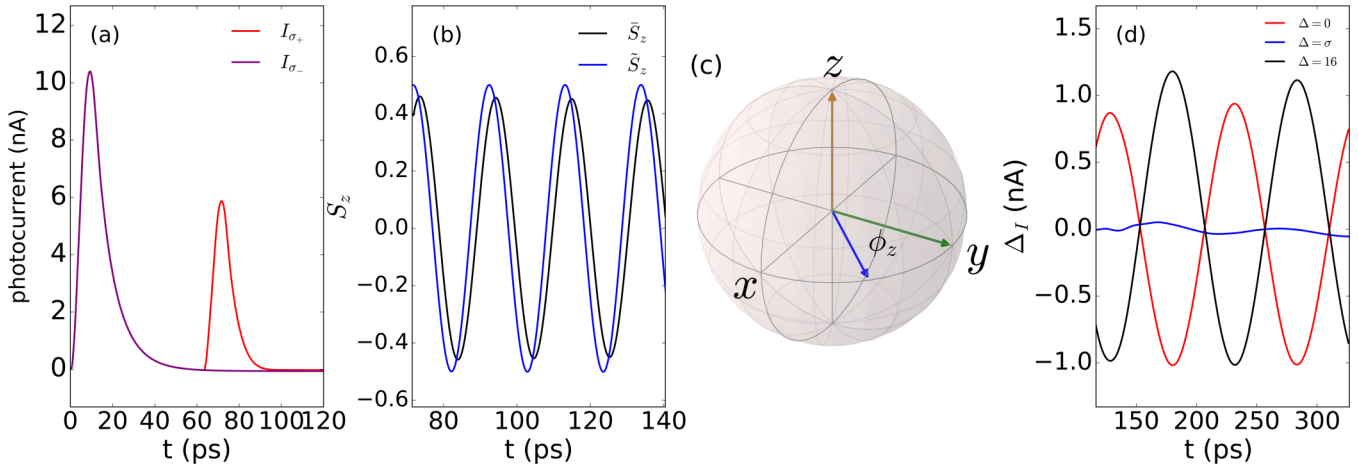

FIG. 3. (a) The real-time photocurrent $I_{\sigma\pm}$ in the presence of magnetic field $B_x = 4.6$ T. The initialization pulse ends at $t = 10$ ps. With a cocircular excitation detection pulse applied at the time delay $\tau_d = \pi/f_L$, no detection photocurrent is produced, while with a cross-circular pulse, detection current is produced. (b) Comparison of the z component of the single-hole spin calculated by $\bar{S}_z$ and $\tilde{S}_z$. (c) Schematic diagram of SU(2) control of a hole spin. The hole spin is the initialization to an up-spin state and performs Larmor precession about the x axis. The hole spin points along the $+y$ direction on the arrival of the geometric-phase control pulse. (d) Photocurrent difference $\Delta_I = I_{\sigma+} - I_{\sigma-}$ of $\sigma_\pm$ detection pulses as a function of precession time. The z-axis rotation control is achieved via a geometric-phase pulse, where the photocurrent oscillation amplitude reflects the rotation angle.

$\tilde{S}_z$ and $\bar{S}_z$ at $\Delta_H = 0.0003$ meV. The overall consistency between them can be seen. Since our theoretical $\tilde{S}_z$ is in good agreement with the experiment data in Ref. [13], the accuracy of the photocurrent readout technique thus has been verified in Fig. 3(b). When the Rabi frequency f_R is comparable to the Zeeman splitting energy of B_x, a small phase difference between $\tilde{S}_z$ and $\bar{S}_z$ appears, as shown in Fig. 3(b). The time evolution of $\tilde{S}_z$ seems slightly behind that of $\bar{S}_z$. That phase difference results from the delay of recording the photocurrent to determine $\tilde{S}_z$. As shown in Fig. 3(a), the photocurrent reaches its peak value at the end of the pulse, when the hole spin has already undergone a precession. By using the parameters of Rabi frequency $hf_R = 0.1$ meV and Zeeman energy $\Delta E_Z = 0.4$ meV ($B_x = 4.6$ T and $g_h = 1.5$) [29,30], the phase delay is of the same magnitude as the half Rabi cycle $T_R/2 \sim 5$ ps, as shown in Fig. 3(b).

In order to realize SU(2) control of the hole spin, a control pulse is needed to rotate the spin along the second rotation axis. Here, we adopt the geometric-phase approach, which was first proposed in theory [26,31] and then successfully realized in experiments [13,32,33]. The control pulse is shaped with a hyperbolic secant envelope to rotate the hole spin about the beam path of the laser (z axis). $H_{\rm opt} = \Omega \mathrm{sech}(\sigma t)(e^{i\omega t} c^\dagger_{c\uparrow} c_{v\downarrow} +$ H.c.), where Ω denotes the Rabi frequency and σ is the bandwidth of the pulse. The σ_- polarized pulse with 2π pulse area drives the Rabi rotation between the single-hole spin state $|\Uparrow\rangle$ and the trion one $|X^+_{\uparrow\Downarrow\Uparrow}\rangle$. In our calculations, $\sigma = \Omega = 0.2$ meV is fixed to guarantee no population transfers to the trion state. The single-hole spin state returns to itself and acquires a phase factor $\phi_z = \arctan(\frac{2\sigma\Delta}{\Delta^2-\sigma^2})$ about the z axis via varying detuning Δ from the resonance between $|\Uparrow\rangle$ and $|X^+_{\uparrow\Downarrow\Uparrow}\rangle$ [31], as schematically illustrated in Fig. 1(b).

To be more concrete, the geometric-phase control pulse is applied at the time delay $\tau = 27$ ps when the hole spin points along the $+y$ axis. Since the rotation radius is equal to that of the Bloch sphere, as shown in Fig. 3(c), the effect of the pulse on the hole spin is the maximum. Carrying the rotation angle ϕ_z, the hole spin continues to precess along the x axis under the B_x magnetic field, with the rotation radius being determined by ϕ_z. Since the detection photocurrent is proportional to the z-axis projection of the hole spin, one can use the photocurrent difference $\Delta_I = I_- - I_+$ between $\sigma_\pm$ detection pulses to pick up information about ϕ_z. The hole spin precession with different Δ is shown in Fig. 3(d), which is very consistent with the experimental curves in Ref. [13]. In Fig. 3(d), the $\sigma_\pm$ detection pulses scan through the precession of the hole spin, and the values of detuning are set to $\Delta = 0, \sigma, 16$ meV, respectively. At $\Delta = \sigma$, the rotation angle is $\pi/2$, which aligns the spin along the $+x$ axis. As a consequence, the precession is maximally suppressed, characterized by a near-constant photocurrent with little oscillation. $\Delta = 0$ and 16 meV correspond to the rotation angle $\phi = 0$ and π, respectively, and the precession radius reaches the maximum values for both cases, which results in significant oscillations of the photocurrent with a phase difference of π, as shown in Fig. 3(d).

IV. SUMMARY AND CONCLUDING REMARKS

In summary, by accurately solving the extended Anderson impurity model in the real-time domain with the HEOM approach, we precisely simulated the whole process of single-hole spin control, including initialization, SU(2) rotation, and readout. Our theoretical results are in good agreement with recent experimental observations, which demonstrates the feasibility and accuracy of the HEOM approach to describe the hole spin dynamics. Particularly, the influence of the hybridization strength on electrodes is fully considered, and a maximal fidelity in the initialization is predicted.

We would like to compare our results with those of an electron spin qubit. The coherence time T_2^* derived from our model calculations (by fitting the decay of the single hole) is about several nanoseconds, much longer than that of electron spin qubits reported in the literature [34,35]. In experiments, T_2^* may be further improved by more delicate setups. Besides the long coherence time, another advantage of a hole spin qubit is the convenience of readout via the photocurrent, as has been demonstrated in experiments and our theory. Relatively, the single-shot electron spin readout is rather challenging in experiments. As for the fidelity, we have illustrated that it can be optimized by adjusting experimental parameters. Finally, we comment that almost all of the techniques developed for electron spins can be used for hole ones since the physical mechanisms underpinning ultrafast optical control of the latter are essentially identical to those of the former.

ACKNOWLEDGMENTS

The support from the NSF of China (Grants No. 11374363 and No. 11774418) and the Research Funds of Renmin University of China (Grant No. 11XNJ026) is gratefully appreciated.

[1] D. Brunner, B. D. Gerardot, P. A. Dalgarno, G. Wüst, K. Karrai, N. G. Stoltz, P. M. Petroff, and R. J. Warburton, Science **325**, 70 (2009).
[2] D. Press, T. D. Ladd, B. Y. Zhang, and Y. Yamamoto, Nature (London) **456**, 218 (2008).
[3] K. De Greve, P. L. McMahon, D. Press, T. D. Ladd, D. Bisping, C. Schneider, M. Kamp, L. Worschech, S. Höfling, A. Forchel *et al.*, Nat. Phys. **7**, 872 (2011).
[4] A. Vamivakas, C.-Y. Lu, C. Matthiesen, Y. Zhao, S. Fält, A. Badolato, and M. Atatüre, Nature (London) **467**, 297 (2010).
[5] A. Delteil, W. B. Gao, P. Fallahi, J. Miguel-Sanchez, and A. Imamoğlu, Phys. Rev. Lett. **112**, 116802 (2014).
[6] I. T. Vink, K. C. Nowack, F. H. Koppens, J. Danon, Y. V. Nazarov, and L. M. Vandersypen, Nat. Phys. **5**, 764 (2009).
[7] J. Fischer, W. A. Coish, D. V. Bulaev, and D. Loss, Phys. Rev. B **78**, 155329 (2008).
[8] P. Fallahi, S. T. Yılmaz, and A. Imamoğlu, Phys. Rev. Lett. **105**, 257402 (2010).
[9] E. A. Chekhovich, A. B. Krysa, M. S. Skolnick, and A. I. Tartakovskii, Phys. Rev. Lett. **106**, 027402 (2011).
[10] P.-L. Ardelt, T. Simmet, K. Müller, C. Dory, K. A. Fischer, A. Bechtold, A. Kleinkauf, H. Riedl, and J. J. Finley, Phys. Rev. B **92**, 115306 (2015).
[11] T. M. Godden, J. H. Quilter, A. J. Ramsay, Y. Wu, P. Brereton, I. J. Luxmoore, J. Puebla, A. M. Fox, and M. S. Skolnick, Phys. Rev. B **85**, 155310 (2012).
[12] B. D. Gerardot, D. Brunner, P. A. Dalgarno, P. Öhberg, S. Seidl, M. Kroner, K. Karrai, N. G. Stoltz, P. M. Petroff, and R. J. Warburton, Nature (London) **451**, 441 (2008).
[13] T. M. Godden, J. H. Quilter, A. J. Ramsay, Y. Wu, P. Brereton, S. J. Boyle, I. J. Luxmoore, J. Puebla-Nunez, A. M. Fox, and M. S. Skolnick, Phys. Rev. Lett. **108**, 017402 (2012).
[14] T. M. Godden, S. J. Boyle, A. J. Ramsay, A. Fox, and M. Skolnick, Appl. Phys. Lett. **97**, 061113 (2010).
[15] A. J. Brash, L. M. P. P. Martins, F. Liu, J. H. Quilter, A. J. Ramsay, M. S. Skolnick, and A. M. Fox, Phys. Rev. B **92**, 121301(R) (2015).
[16] D. Heiss, V. Jovanov, M. Bichler, G. Abstreiter, and J. J. Finley, Phys. Rev. B **77**, 235442 (2008).
[17] H.-P. Breuer and F. Petruccione, *The Theory of Open Quantum Systems* (Oxford University Press, Oxford, 2002).
[18] J. S. Jin, X. Zheng, and Y. J. Yan, J. Chem. Phys. **128**, 234703 (2008).
[19] Z. H. Li, N. H. Tong, X. Zheng, D. Hou, J. H. Wei, J. Hu, and Y. J. Yan, Phys. Rev. Lett. **109**, 266403 (2012).
[20] L. Z. Ye, X. L. Wang, D. Hou, R. X. Xu, X. Zheng, and Y. J. Yan, WIREs Comput. Mol. Sci. **6**, 608 (2016).
[21] R. Härtle, G. Cohen, D. R. Reichman, and A. J. Millis, Phys. Rev. B **92**, 085430 (2015).
[22] X. Zheng, Y. J. Yan, and M. Di Ventra, Phys. Rev. Lett. **111**, 086601 (2013).
[23] Y. X. Cheng, Y. D. Wang, J. H. Wei, Z. G. Zhu, and Y. J. Yan, Phys. Rev. B **95**, 155417 (2017).
[24] W. J. Hou, Y. D. Wang, J. H. Wei, and Y. J. Yan, J. Chem. Phys. **146**, 224304 (2017).
[25] W. J. Hou, Y. D. Wang, J. H. Wei, Z. G. Zhu, and Y. J. Yan, Sci. Rep. **7**, 2468 (2017).
[26] S. E. Economou and T. L. Reinecke, Phys. Rev. Lett. **99**, 217401 (2007).
[27] J. D. Mar, J. J. Baumberg, X. L. Xu, A. C. Irvine, C. R. Stanley, and D. A. Williams, Phys. Rev. B **87**, 155315 (2013).
[28] J. F. Poyatos, J. I. Cirac, and P. Zoller, Phys. Rev. Lett. **78**, 390 (1997).
[29] F. Fras, B. Eble, P. Desfonds, F. Bernardot, C. Testelin, M. Chamarro, A. Miard, and A. Lemaître, Phys. Rev. B **84**, 125431 (2011).
[30] B. Eble, P. Desfonds, F. Fras, F. Bernardot, C. Testelin, M. Chamarro, A. Miard, and A. Lemaître, Phys. Rev. B **81**, 045322 (2010).
[31] S. E. Economou, L. J. Sham, Y. Wu, and D. G. Steel, Phys. Rev. B **74**, 205415 (2006).
[32] E. D. Kim, K. Truex, X. Xu, B. Sun, D. G. Steel, A. S. Bracker, D. Gammon, and L. J. Sham, Phys. Rev. Lett. **104**, 167401 (2010).
[33] A. Greilich, S. E. Economou, S. Spatzek, D. Yakovlev, D. Reuter, A. Wieck, T. Reinecke, and M. Bayer, Nat. Phys. **5**, 262 (2009).
[34] X. D. Xu, B. Sun, P. R. Berman, D. G. Steel, A. S. Bracker, D. Gammon, and L. J. Sham, Nat. Phys. **4**, 692 (2008).
[35] W. Gao, P. Fallahi, E. Togan, J. Miguel-Sánchez, and A. Imamoglu, Nature (London) **491**, 426 (2012).